Accurate quantum dynamics simulation of the photodetachment spectrum of the nitrate anion (NO_3^-) based on an artificial neural network diabatic potential model

Alexandra Viel, David M. G. Williams, and Wolfgang Eisfeld

COLLECTIONS

Paper published as part of the special topic on Quantum Dynamics with ab Initio Potentials

View Online   Export Citation   CrossMark

ARTICLES YOU MAY BE INTERESTED IN

Potential energy surfaces for high-energy N + O_2 collisions
The Journal of Chemical Physics **154**, 084304 (2021); https://doi.org/10.1063/5.0039771

Vibrational quenching of CN^- in collisions with He and Ar
The Journal of Chemical Physics **154**, 084305 (2021); https://doi.org/10.1063/5.0039854

Explicit environmental and vibronic effects in simulations of linear and nonlinear optical spectroscopy
The Journal of Chemical Physics **154**, 084116 (2021); https://doi.org/10.1063/5.0038196
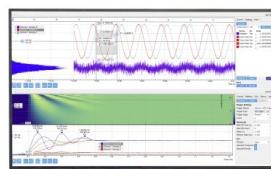
Accurate quantum dynamics simulation of the photodetachment spectrum of the nitrate anion (NO₃⁻) based on an artificial neural network diabatic potential model

View Online   Export Citation   CrossMark

Alexandra Viel,[a]   David M. G. Williams,[2,b]   and Wolfgang Eisfeld[2,c]

AFFILIATIONS

[1] University Rennes, CNRS, IPR (Institut de Physique de Rennes) - UMR 6251, F-35000 Rennes, France

[2] Theoretische Chemie, Universität Bielefeld, Postfach 100131, D-33501 Bielefeld, Germany

Note: This paper is part of the JCP Special Topic on Quantum Dynamics with *Ab Initio* Potentials.
[a] alexandra.viel@univ-rennes1.fr
[b] d.williams@uni-bielefeld.de
[c] **Author to whom correspondence should be addressed:** wolfgang.eisfeld@uni-bielefeld.de

ABSTRACT

The photodetachment spectrum of the nitrate anion (NO_3^-) is simulated from first principles using wavepacket quantum dynamics propagation and a newly developed accurate full-dimensional fully coupled five state diabatic potential model. This model utilizes the recently proposed complete nuclear permutation inversion invariant artificial neural network diabatization technique [D. M. G. Williams and W. Eisfeld, J. Phys. Chem. A **124**, 7608 (2020)]. The quantum dynamics simulations are designed such that temperature effects and the impact of near threshold detachment are taken into account. Thus, the two available experiments at high temperature and at cryogenic temperature using the slow electron velocity-map imaging technique can be reproduced in very good agreement. These results clearly show the relevance of hot bands and vibronic coupling between the $\tilde{X}$ $^2A_2'$ ground state and the $\tilde{B}$ $^2E'$ excited state of the neutral radical. This together with the recent experiment at low temperature gives further support for the proper assignment of the ν_3 fundamental, which has been debated for many years. An assignment of a not yet discussed hot band line is also proposed.

Published under license by AIP Publishing. https://doi.org/10.1063/5.0039503

I. INTRODUCTION

One central goal of chemical physics is the detailed and fundamental understanding of the nuclear dynamics of molecular systems. Impressive progress has been achieved in this quest by the combined efforts of experiment and theory over the past few decades. Yet, there are still enigmatic systems that, despite being studied intensively, are not understood very well. The nitrate radical (NO_3) is one such case, which, on the one hand, is of high significance due to its importance in atmospheric chemistry[1] and, on the other hand, shows complicated nuclear dynamics and correspondingly complex spectra. This

sparked the interest of many research groups over the years both experimentally[2-40] and theoretically.[41-75]

One of the reasons for the complicated behavior of NO_3 seems to be the presence of strong nonadiabatic coupling effects. The two first electronically excited states are of $^2E''$ and $^2E'$ symmetry, respectively, and thus are subject to an $E \otimes e$ Jahn–Teller (JT) effect. The leading linear JT coupling causes a conical intersection in D_{3h} symmetric nuclear configurations, which induces a geometric phase in the adiabatic representation due to the singularity of the nonadiabatic coupling. This results in very complicated spectra corresponding to the excited state manifolds. But even the

non-degenerate ground state of $^2A_2'$ symmetry shows spectroscopic features that have been debated for decades. This may be attributed at least in part to significant vibronic couplings to the excited state manifolds. A further complication is that NO_3 is difficult to study both experimentally and theoretically. The bottleneck for detailed theoretical studies of the nuclear dynamics and spectroscopy is the need for a very accurate potential energy surface (PES) model based on advanced electronic structure calculations. Various models have been developed in the past,[40,64–68,70–75] but it has been a stony track to achieve the required quality to reach decisive interpretations in comparison with experimental observations. Our recent developments for producing highly accurate diabatic PES models using artificial neural networks (ANNs) should be a significant step forward to reach that goal.[76–78]

One experimental breakthrough has been the first photodetachment spectrum of the nitrate anion (NO_3^-) published by the Neumark group in 1991.[34] This has been the first direct experimental proof of the existence of the $\tilde{A}\,^2E''$ state of the radical, which previously only had been predicted by theory.[79] This experiment also provided new data for the $\tilde{X}\,^2A_2'$ state of the radical. However, both partial spectra showed idiosyncrasies that sparked the discussion of their interpretation. A very recent experiment from the same group tried to resolve at least some questions regarding the $\tilde{X}$ state.[80] By cryogenic cooling, some hot bands of the original spectrum could be removed, which allows us to focus on the remaining unexpected features more clearly. Unfortunately, a corresponding experiment for the $\tilde{A}$ state is not available yet. Thus, one aim of the present study is to simulate the temperature effects on the spectra theoretically and to compare the results with the new experimental data available.

Several attempts to simulate this experiment have been published over the years.[64,71–73,80] While the $\tilde{X}$ state could be simulated reasonably well even in the first attempt,[64] the $\tilde{A}$ state took a lot more effort and required a lot of development to obtain a sufficiently accurate PES model.[73,81–84] Further development enables us now to use a PES model of unprecedented accuracy to simulate the corresponding spectra.[76–78,85–87]

II. FULLY COUPLED DIABATIC 6D POTENTIAL ENERGY MODEL

The basic idea behind the model potential used in the present work is presented here briefly, and for a deeper discussion, we refer the interested reader to Ref. 78. The quantum dynamics of NO_3 is strongly influenced by (vibronic) coupling among several electronic states, and thus, a diabatic representation of the PES model is chosen. One benefit of this choice is that the functional form of the diabatic matrix elements is rather simple, and another advantage is that the geometric phase effect is taken care of properly.[87] The disadvantage is that diabatic representations are neither unique nor directly accessible. For this reason, an established low-order vibronic coupling expansion of the electronic Hamiltonian is utilized as a reference model, which ensures that the diabatic model is physically meaningful.[88,89] That model is not very accurate, though, and thus, it is only used as a reference model. The expansion coefficients of that model are tuned depending on the nuclear coordinates by an artificial neural network (ANN). This

newly developed method was shown to result in highly accurate and reliable diabatic PES models for planar (5D) NO_3.[76–78] The extension of our approach to the full-dimensional (6D) diabatic PES model for NO_3 is presented here. The underlying *ansatz* for the diabatic matrix is expressed as a sum of diagonal and coupling matrices[76,82,89] reading

$$
\begin{aligned}
\mathbf{W}^d(\mathbf{Q}) = \mathbf{W}^d_{diag}(\mathbf{Q}) &+ \begin{pmatrix} \lambda_1 & 0^T & 0^T \\ 0 & \lambda_2\mathbf{1} & 0 \\ 0 & 0 & \lambda_3\mathbf{1} \end{pmatrix} + \theta \cdot \begin{pmatrix} 0 & 0^T & 0^T \\ 0 & 0 & \lambda_{10}\mathbf{1} \\ 0 & \lambda_{10}\mathbf{1} & 0 \end{pmatrix} \\
&+ \begin{pmatrix} 0 & 0^T & \lambda_8\boldsymbol{\rho}_s{}^T + \lambda_9\boldsymbol{\rho}_b{}^T \\ 0 & \lambda_4\boldsymbol{\varepsilon}_s + \lambda_5\boldsymbol{\varepsilon}_b & 0 \\ \lambda_8\boldsymbol{\rho}_s + \lambda_9\boldsymbol{\rho}_b & 0 & \lambda_6\boldsymbol{\varepsilon}_s + \lambda_7\boldsymbol{\varepsilon}_b \end{pmatrix} \\
&+ \theta \cdot \begin{pmatrix} 0 & \lambda_{11}\boldsymbol{\rho}_s{}^T + \lambda_{12}\boldsymbol{\rho}_b{}^T & 0^T \\ \lambda_{11}\boldsymbol{\rho}_s + \lambda_{12}\boldsymbol{\rho}_b & 0 & \lambda_{13}\boldsymbol{\varepsilon}_s + \lambda_{14}\boldsymbol{\varepsilon}_b \\ 0 & \lambda_{13}\boldsymbol{\varepsilon}_s + \lambda_{14}\boldsymbol{\varepsilon}_b & 0 \end{pmatrix},
\end{aligned}
\tag{1}
$$

where $\mathbf{W}^d_{\text{diag}}(\mathbf{Q})$ is a diagonal matrix that contains first and second order terms as detailed in previous work[73,75,76,83] and reproduced in the Appendix. $\mathbf{W}^d_{\text{diag}}(\mathbf{Q})$ can be considered an average potential for the degenerate states and is composed of purely polynomial terms. The first explicitly given matrix in Eq. (1), where $\mathbf{1}$ means the 2×2 unit matrix, corresponds to the diagonal correction potential for states $^2A_2'$, $^2E''$, and $^2E'$. The second matrix represents the totally symmetric part of the inter-state coupling between the $^2E''$ and $^2E'$ states, while the fourth matrix stands for the non-totally symmetric inter-state couplings. These two matrices couple pairs of states of different symmetry with respect to the σ_h symmetry operator. Due to symmetry, all inter-state couplings between states of (A', E') and E'' symmetry, respectively, are proportional to the umbrella coordinate θ and, hence, vanish for planar geometries. The third matrix contains the well-known JT couplings within the two degenerate states and the *pseudo*-JT couplings between the $\tilde{X}$ and $\tilde{B}$ state. The 2×2 matrices $\boldsymbol{\varepsilon}_{s,b}$ in Eq. (1) are the first-order Jahn–Teller coupling blocks, and the vectors $\boldsymbol{\rho}_{s,b}$ are the pseudo-Jahn–Teller coupling blocks given by

$$
\boldsymbol{\varepsilon}_{s,b} = \begin{pmatrix} x_{s,b} & y_{s,b} \\ y_{s,b} & -x_{s,b} \end{pmatrix} \quad \text{and} \quad \boldsymbol{\rho}_{s,b} = \begin{pmatrix} y_{s,b} \\ x_{s,b} \end{pmatrix},
\tag{2}
$$

where $x_{s,b}$, $y_{s,b}$, and θ are symmetry-adapted coordinates corresponding to the degenerate asymmetric stretching (s) and bending (b) modes ($x_{s,b}$, $y_{s,b}$) and the umbrella motion (θ). These coordinates together with the symmetric stretch coordinate a are gathered in the 6D vector of nuclear coordinates $\mathbf{Q}$. They are defined identically to those used in previous studies[73,83] and provided in the Appendix for the sake of convenience.

The key for the accuracy of the present model is that the vibronic coupling coefficients, $\lambda_j(\mathbf{Q})$ [$j = 1, \ldots 14$] in Eq. (1), are not constants like in standard vibronic coupling models. Instead, they depend on all six nuclear coordinates $\mathbf{Q}$ through the use of an ANN with the coordinates as the input layer (see below). In fact, the

standard vibronic coupling constants are first fitted to yield a low order reference model, which describes the diabatic Hamiltonian qualitatively correctly and reasonably well. Then, an ANN is trained, which depends on the coordinates and yields output neurons, which modulate the coupling constants. More specifically, the modified j depend on invariant functions, $\widetilde{\mathbf{Q}}$, constructed from $\mathbf{Q}$. The use of the invariants ensures maintaining the correct symmetry and was found to be the most accurate and efficient use of the ANN as shown in recent work.[77] Apart from the inclusion of θ^2 to account for the additional degree of freedom, the invariants ($\widetilde{\mathbf{Q}}$) are identical to those used for the 5D ANN-based model described in Ref. 78. These invariants are provided in the Appendix for the convenience of the reader.

The new 6D model is constructed such that for $\theta = 0$, the 5D ANN model from Ref. 78 is reproduced exactly. To this end, the vibronic coupling constants of a reference model λ_j^0 are tuned by the scaled output neurons $\eta_j^{5D}(\widetilde{\mathbf{Q}})$. In addition, since the umbrella coordinate is now present, a second ANN, yielding the output neurons $\eta_j^{6D}(\widetilde{\mathbf{Q}})$, is introduced to provide the necessary θ-dependence to the λ_j parameters. More specifically, the coefficients λ_{1-3}^0, which correspond to the adiabatic energies at the reference point, are made coordinate-dependent by

$$\lambda_j(\widetilde{\mathbf{Q}}) = \lambda_j^0 \cdot \left(1 + c_j^{5D} \cdot \eta_j^{5D}(\widetilde{\mathbf{Q}}) + \theta^2 \cdot c_j^{6D} \cdot \eta_j^{6D}(\widetilde{\mathbf{Q}})\right) \quad \forall j \leq 3, \quad (3)$$

and the coefficients λ_{4-9}, also present in the 5D model, are constructed similarly,

$$\lambda_j(\widetilde{\mathbf{Q}}) = \lambda_j^0 \cdot \left(1 + c_j^{5D} \eta_j^{5D}(\widetilde{\mathbf{Q}}) + \theta^2 \cdot c_j^{6D} \cdot \eta_j^{6D}(\widetilde{\mathbf{Q}})\right), \quad 4 \leq j \leq 9, \quad (4)$$

where η_j^{6D} are the outputs of the additional neural network depending on $\widetilde{\mathbf{Q}}$, which account for the effects of non-planar geometries. The ANN yields the best results if the output neurons reside roughly within an interval of $[-1, 1]$. Usually, the function values to be encoded by the output neurons do not fall within this range or even order of magnitude. For this reason, the output neurons are scaled by appropriate scaling factors before the ANN is trained. This approach improves the convergence of the training and reduces the remaining error considerably as was shown before.[76] Since the full 6D model is a combination of two different ANNs, there are also two sets of scaling factors c_j^{5D} and c_j^{6D}, respectively. The additional parameters λ_{10-14} are defined in analogy to the previously utilized models and correct the new inter-state coupling terms, which vanish for planar geometries and, thus, were not included in the previous 5D models. These read

$$\lambda_j(\widetilde{\mathbf{Q}}) = \lambda_j^0 \cdot \left(1 + c_j^{6D} \cdot \eta_j^{6D}(\widetilde{\mathbf{Q}})\right) \ \forall j \geq 10. \quad (5)$$

The constants λ_j^0 are obtained from non-linear least squares fits with respect to accurate *ab initio* reference data and yield a qualitatively correct reference model. In a second step, the two ANNs are trained with respect to the same reference data and provide the $\mathbf{Q}$-dependent corrections. A global view of the above equations is that the λ_j coefficients are actually modified not by a single but by *two* ANNs, the original θ-independent 5D model from Ref. 78, $\eta_j^{5D}(\widetilde{\mathbf{Q}})$, and the neurons η_j^{6D} from the ANN used in Eq. (5).

The advantage of this approach is that the previously derived 5D ANN model,[78] which is of excellent quality, is available already and accounts for a large part of the full 6D model. Equations (3)–(5) ensure that the coefficients λ_j are constructed in such a way that the model smoothly falls back to the original 5D model for planar geometries. In this way, the present, full-dimensional model naturally extends the previous planar model by including out-of-plane motions, while simultaneously correcting the additional contributions of the new vibronic coupling terms. This further serves as a proof of concept that the previously established scheme can be extended without the need of changing the general structure of the *ansatz*.

All neural networks involved in the construction of the model belong to the broad category of feed-forward neutral networks. They are functions taking a vector $\widetilde{\mathbf{Q}} = \boldsymbol{\eta}^{(1)}$ as input and processing it via intermediate results $\boldsymbol{\eta}^{(k)}$, the so-called hidden layers, to a final (L^{th}) output vector $\boldsymbol{\eta}^{(L)} = \boldsymbol{\eta}^{6D}$ called the output layer. The vector elements of each layer are called *neurons*. Each intermediate $\boldsymbol{\eta}(k)$ depends solely on the previous layer $\boldsymbol{\eta}^{(k-1)}$ by

$$\eta_j^{(k)} = f^k \left(\beta_j^{(k)} + \sum_l \omega_{jl}^{(k)} \eta_l^{(k-1)} \right), \quad (6)$$

where $f^{(k)}$ is a nonlinear function of one variable called the *activation function*. In the present case, $f^{(k)}$ is chosen to be tanh for the single unique hidden layer $k = 2$ and as the identity Id for the output ($k = 3$). $\omega_{jl}^{(k)}$ and $\beta_j^{(k)}$ are called *weights* and *biases*, respectively. They are the fitting parameters of the neural network.

The additional neural network accounting for the θ-dependence of the 6D model contains a single hidden layer with ten hidden layer neurons, corresponding to a function of ~250 formal parameters. While significantly larger (and smaller) networks have been tested, this network size is considered the most suitable. As in our previous work,[76] this ANN was trained for a set of 100 random initial guesses using a specialized ANN Marquardt-Levenberg method developed in-house. The dataset is composed of over 2400 (non-planar) geometries, with a validation dataset of about 400 additional geometries. This is a significantly smaller dataset than that was used for planar geometries (18 000 geometries), as accurate *ab initio* data for fully asymmetrical (C_1) geometries are significantly more expensive and problematic to attain. All *ab initio* reference data were computed using internally contracted multi-configuration reference singles double configuration interaction[90,91] (MR-SDCI) and a hand tailored basis of augmented triple zeta quality. These calculations were performed using the Molpro program package.[92] Full details about the electronic structure setup can be found in Refs. 61, 62, and 73.

The reference model (including the previous 5D ANN and fitted $\lambda_j^{(0)}$) yields a root mean square (rms) error of 835 cm^{-1}, which is significantly higher than the final error after the ANN training of 58.1 cm^{-1}. This fitting error only includes non-planar geometries, as the model is identical to the previous 5D model for planar geometries. Most likely, this increase in the rms error is due to the less reliable *ab initio* reference data. The internally contracted MR-SDCI calculations for unsymmetric NO$_3$ configurations are not only extremely time consuming but also

rather involved. For instance, the reference states may change character and/or active orbitals from the underlying complete active space self-consistent field (CASSCF) calculations may rotate for strongly distorted geometries. Such problems are less pronounced if symmetry restrictions can be applied to the electronic wave function. For this reason, all data were acquired along straight cuts through six-dimensional nuclear coordinate space (NCS). This allows for careful analysis to pinpoint data points with convergence problems by their obvious deviation from the predicted energies or by block-diagonalization techniques.[85] However, it cannot be guaranteed that really all points with convergence issues are detected and removed from the reference set. We infer that their potential and likely presence may give rise to higher rms errors.

A discussion of more technical matters such as potential benefits of using "deeper" neural networks with more hidden layers or the size of the reference dataset have been discussed at great length in previous studies[76–78] and, hence, will not be repeated here.

III. COMPUTATIONAL DETAILS

The aim of the present study is to unravel the effects of temperature (hot bands) and vibronic coupling in the low energy regime of the photodetachment spectrum by accurate quantum dynamics simulations. To this end, a time-dependent approach is used for the determination of the detachment spectrum. More specifically, the propagation of a six-dimensional wavepacket evolving on the five coupled PESs of the radical is performed starting from the eigenfunction of each of the lowest vibrational states of NO_3^-. The spectra obtained from the Fourier transform of the resulting autocorrelation functions are subsequently added with the proper Boltzmann weights to simulate the NO_3^- photodetachment spectrum at a given temperature. The Multi-configuration Time-dependent Hartree (MCTDH) approach,[93,94] suitable for the representation of wave functions with large dimensionality, is employed for the time propagation of the wavepackets. The state average and block diagonalization schemes[95] are used for the determination of the vibrational eigenfunctions of the anion.

The six internal curvilinear coordinates $\rho^{(cu)}$, $\vartheta^{(cu)}$, $\varphi^{(cu)}$, $\theta^{(cu)}$, $\phi^{(cu)}$, and $\chi^{(cu)}$, as proposed in Ref. 96, are used in the dynamics calculations. The associated *quasi*-exact kinetic operator is approximated by the fourth order Taylor expansion as detailed in Ref. 96. Both our previous studies[74,75] on the first excited state of NO_3 and on the computation of the vibronic levels of the ground state of NO_3 have demonstrated that this choice of coordinates and approximation is efficient and suitable for the study of the NO_3 radical. In the MCTDH approach used, the evaluation of the potential term is carried out using the CDVR scheme[97] for the anion and using the generalized version as detailed in the Appendix of Ref. 83 for the evaluation of the diabatic five by five potential matrix of the radical.

The dominant low energy part of the photodetachment experiments[34,80] is simulated by assuming a vertical transition of one of the NO_3^- vibrational eigenfunctions onto the lowest component corresponding to the $^2A_2'$ state of the diabatic potential matrix of the neutral system. An additional signal is obtained in the low energy

domain from the vertical transition to the two E′ components of the diabatic model. This second contribution is clearly due to vibronic coupling between the $^2A_2'$ ground and $^2E'$ excited electronic state of the radical. No significant signal is found in the same energy range when the vertical transition to the two $^2E''$ components is treated. A propagation time of 250 fs is found to be sufficient for the comparison of the computed spectrum with the experimental data.

Table I provides the numerical details of the basis set used for the representation of the wavepackets. Careful attention was paid to the definition of the underlying box, to the number of single particle functions n, and the number of Fourier grid points N to ensure a converged autocorrelation function up to the relevant propagation time. The basis definition is adapted to the excitation to the E′ components. A smaller basis would be sufficient for the case of a vertical transition to the lowest diabatic PES only.

The lowest vibrational energy levels of the anion[73] and their contribution to the final spectrum by means of Boltzmann weights for 435 K as in the experimental work[34] are presented in Table II. At 10 K, the only relevant initial vibrational state is the ground state.

When comparing with the experimental data, one must keep in mind the current limits of the theoretical approach. First, no overall rotation is taken into account explicitly. The width of the peaks is introduced by an *ad hoc* damping of the autocorrelation function to be Fourier transformed. Second, no *ab initio* information about the photo-detachment cross section is used. In usual absorption spectroscopy, the dipole operator could be modeled using *ab initio* data. No comparable data are available in the present case of electron detachment because we have no way to evaluate the dipole matrix elements between the anion initial state and the radical plus free electron final state. As a substitute, an arbitrary relative weight of the two different electronic state manifolds is used to match the measured spectra of the two experimental setups. Finally, the presented computing time and memory demanding computations of the E′ manifold correspond to a low intensity part of the full spectrum and are, thus, more sensitive to round off errors. Extensive convergence tests were performed to ensure that the presented data discussed in the following are not artificial.

TABLE I. Wave function representations given by the number of single particle functions (n), the number of Fourier points (N), and the range of the underlying box (in a.u.) for the six curvilinear coordinates of hyperspherical type constructed using mass weighted Cartesian coordinates.

Coord.	N	N	Range
$\rho^{(cu)}$	8	64	[635:840]
$\vartheta^{(cu)}$	9	96	[0.785:1.055]
$\varphi^{(cu)}$	9	64	[0.615:0.955]
$\theta^{(cu)}$	6	32	[1.431:1.711]
$\phi^{(cu)}$	10	96	[0.820:1.295]
$\chi^{(cu)}$	10	64	[2.809:3.474]
Electronic	5	5	

TABLE II. Ground state energy with respect to the bottom of the potential energy surface and excitation energies for the first six vibrational states of NO_3^- in cm^{-1}. The Boltzmann weights, $B_i = \exp(-E/k_BT)$, at 435 K are also given in units of B_1.

Level	Description	E_i (cm^{-1})	B_i/B_1
1	Ground state	0(3038)[a]	1
2	Antisym bending	703	0.10
3	Antisym bending	703	0.10
4	Umbrella	845	0.06
5	Sym stretching	1040	0.03
6	Antisym stretching	1353	0.01
7	Antisym stretching	1353	0.01

[a]Zero-point energy in parentheses.

IV. RESULTS AND DISCUSSION

The present quantum dynamics simulations of the photodetachment spectrum of NO_3^- are designed in order to disentangle unequivocally the effects of temperature and vibronic coupling in the observed spectra. The assignment and interpretation of the spectroscopy of the NO_3 anion and the radical gave rise to several controversies over the past few decades. The first photodetachment spectrum published in 1991 was a breakthrough in the understanding of NO_3 and sparked significant interest.[34] The latest slow electron velocity-map imaging (SEVI) experiment[80] carried out at cryogenic temperature and with various photon energies provides a wealth of new information. The present first principles simulations based on the new and highly accurate diabatic PES model are capable of substantiating the interpretations of those experiments and hopefully end at least some of the debate. An overview of the present simulation results in comparison with these two experiments is given in Fig. 1.

The first issue to be addressed for a complete understanding of the photodetachment spectroscopy of NO_3^- is the influence of temperature and the contribution of hot bands to the spectrum. The absence of one prominent feature (**m**) in the new cryogenically cooled spectrum clearly identifies that peak as a hot band. The simulation of the spectrum at a temperature of 435 K, the value estimated from the first photodetachment experiment,[34] reproduces this hot band, labeled **m**, and confirms the original assignment as 4^1_1 transition. From Figs. 1 and 2, it is found that the excellent agreement between theory and experiment becomes obvious.

The full photodetachment spectrum is simulated by two partial spectra corresponding to the contributions of the $\tilde{X}\ ^2A_2'$ and the $\tilde{B}\ ^2E'$ state, respectively. These two partial spectra are also given in Fig. 2 in order to make their contributions to the experimentally observed spectrum more clear. The reason for this approach is that the detachment cross sections corresponding to the two different electronic state manifolds are very different and need to be taken into account. The scaling factors due to these different cross sections and the energy shift due to the lack of size extensivity of the underlying *ab initio* calculations are the only empirical factors used in the present study. The partial spectra are obtained from an initially
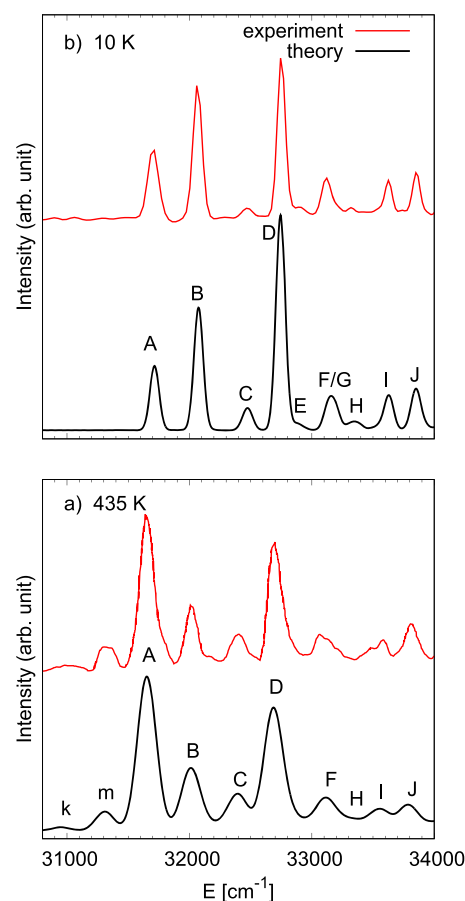

FIG. 1. Comparison of experimental photodetachment spectra with the final quantum dynamics simulation results. Panel (a) presents the theoretical and experimental[34] spectra at an estimated temperature of 435 K. Panel (b) shows results at 10 K in comparison with the new cryo-SEVI results.[80] A damping time of 200 fs (100 fs, respectively) is used for the 10 K (435 K, respectively) theoretical spectra. A ratio of 1/150 (1/30, respectively) is used for the $\tilde{X}\ ^2A_2'$ and the $\tilde{B}\ ^2E'$ partial spectra at 10 K (435 K, respectively).

diabatically pure $\tilde{X}\ ^2A_2'$ or $\tilde{B}\ ^2E'$ vibronic wavepacket. This initial condition relaxes as soon as the propagation starts and the propagated wavepackets acquire non-zero probability in all five coupled electronic states. Each of these partial spectra can be decomposed further into the contributions originating from different thermally populated initial states in the NO_3^- anion.

The detailed and decomposed partial spectrum corresponding to the $\tilde{X}$ state manifold is presented in panel (a) of Fig. 3. The photodetachment spectrum obtained when using the vibrational ground state of the anion after a vertical excitation onto the lowest diabatic component is presented in red. The blue spectra are obtained when the initial wavepacket bears one quantum of energy in the anti-symmetric bending of NO_3^-, and the violet trace is obtained when the initial wavepacket is excited in the umbrella
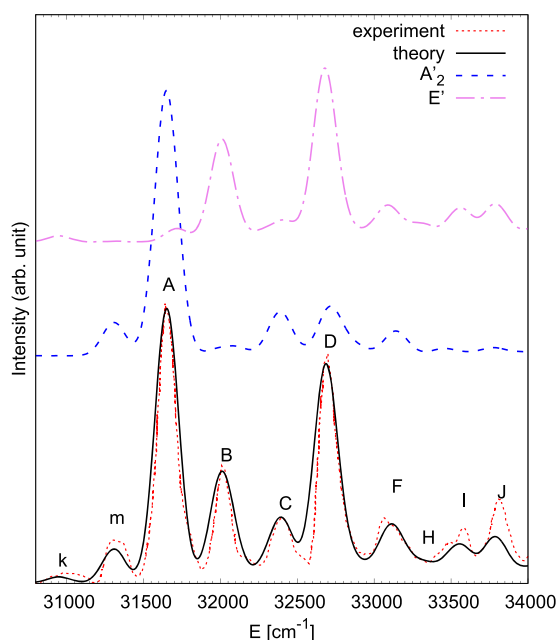
FIG. 2. The theoretically simulated spectrum at T = 435 K (black) is compared with the experimental hot spectrum from Ref. 34 (dotted red). The partial contributions from the $\tilde{X}\ ^2A_2'$ and the $\tilde{B}\ ^2E'$ states are also shown in blue dashed and violet dotted–dashed curves, respectively. The $\tilde{B}\ ^2E'$ contribution is scaled by 30 with respect to the $\tilde{X}\ ^2A_2'$ one.

mode. The black curve is the resulting spectrum considering a temperature of 435 K, thus taking into account the Boltzmann factors of the initial states (see Table II). Because of the lack of size extensivity of the underlying *ab initio* method, the computed absolute energies of the radical and of the anion cannot be compared. For this reason, we present theoretical spectra shifted in energy so that the most intense peak (**A**) obtained matches the experimental data. Only the energy range of the relevant experimental data is shown.

The partial spectra from the wavepacket propagations provide information about the entire progression of the corresponding hot band contributions to the total spectrum at 435 K. Some of these peaks superimpose features of the cold spectrum and may lead to a broadening because of slightly shifted transition energies. This is entirely the case for all contributions when a single v_2 (umbrella) excitation in the anion is considered. Only excitation of v_4 (asymmetric bend) gives rise to additional features clearly distinguishable from peaks in the cold spectrum. Probably, the most interesting of these additional contributions is found at the position of the disputed first peak above the origin 0_0^0 transition labeled **B** in Fig. 1. This feature was attributed to the Franck–Condon (FC) forbidden 4_0^1 transition by Weaver *et al.*[34] but assigned to the FC allowed 4_1^3 hot band transition by Yamada and Ross.[98] The present results clearly show that there is a corresponding hot band transition at this energy, but its intensity is way too small to explain the experimentally observed spectrum. This is also in agreement with the fact that this peak is very prominent in the cryogenically cooled spectrum where hot bands are absent.
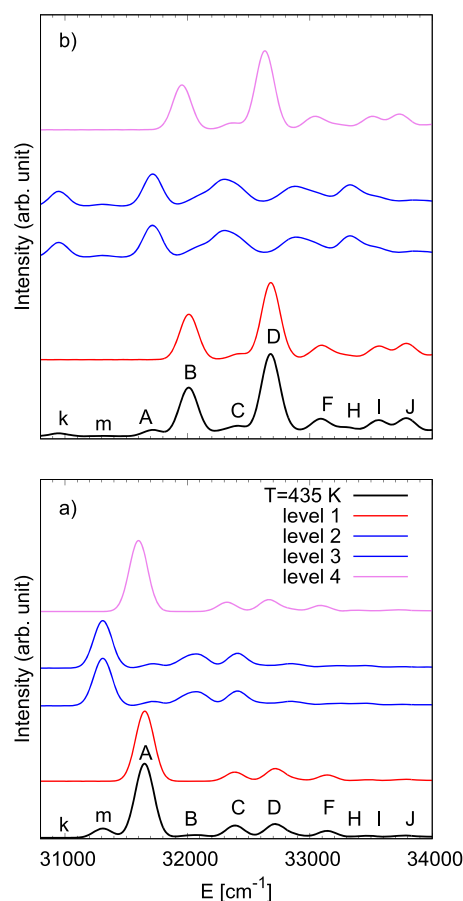

FIG. 3. Partial spectra at 435 K (black) corresponding to excitation to $\tilde{X}\ ^2A_2'$ (a) and to $\tilde{B}\ ^2E'$ (b). The contributions from the different vibrational states of the anion are also displayed: vibrational ground state in red, anti-symmetric bending in blue, and umbrella in violet.

Excitations of the same initial NO_3^- vibrational eigenfunctions to the two $^2E'$ components of NO_3 result in spectra provided in panel (b) of Fig. 3. The vertical axis is not scaled to the same arbitrary unit for the two panels, however. The ground state and the v_2 (umbrella) excitation produce partial spectra with two main peaks. The first is superposed to the 4_1^3 hot band at position **B** (see the blue curve in panel a), which explains the higher intensity of this peak in the final spectrum as seen in Fig. 3.

The second prominent feature of this partial spectrum is found at a position roughly 1040 cm^{-1} above the 0_0^0 peak and was assigned originally to the FC allowed 1_0^1 transition by Weaver *et al.*[34] (labeled **D** in Fig. 1). However, a 1_0^1 transition should not show up in the partial spectrum corresponding to the $\tilde{B}$ state manifold. In fact, we do observe a weak feature slightly to the blue of this peak in the $\tilde{X}$ state partial spectrum, but its intensity would be too low to explain the experimentally observed spectrum. When we compare the peak positions of the partial photodetachment spectra with our earlier studies providing accurate vibrational eigenstate energies for the $\tilde{X}$ manifold, we find that FC allowed 1_0^1 transition should

correspond to about 1056 cm^{-1} above 0_0^0, while the FC forbidden 3_0^1 transition would correspond to about 1036 cm^{-1} above origin. The latter assignment is in agreement with the interpretation of the new cryo-SEVI spectrum.[80] Thus, the main intensity of observed peak **D** apparently originates from the $\tilde{B}$ state manifold and indicates significant vibronic coupling between the two involved electronic states. The present results show that both assignments are correct because the experimentally observed feature is a superposition of both detachment channels.

Some weaker additional features due to the $\tilde{B}$ state manifold are found at higher energies, but they are fairly weak compared to the two very prominent peaks discussed above. The temperature effects can be included in the same way as for the $\tilde{X}$ state manifold, and a similar behavior is found. Hot band contributions due to a single quantum in ν_2 (umbrella) in the initial state yield a spectrum very similar to the one obtained for the sole ground state, the only partial spectrum relevant at cryogenic temperature (10 K). By contrast, a single quantum in ν_4 (asymmetric bend) in the initial state results in a very different spectrum. The first prominent peak is slightly shifted to the blue compared to the origin peak in the $\tilde{X}$ state manifold. Next, there is a fairly broad feature in the region around 32 300 cm^{-1} where there is little intensity originating from the $\tilde{X}$ state manifold. Two similarly broad features are observed above around 32 880 cm^{-1} and 33 330 cm^{-1}.

At lower energy, one very interesting observation is some intensity around 31 000 cm^{-1} and, thus, about 700 cm^{-1} below the 0_0^0 origin peak of the experimental spectrum. Apparently, this is a hot band due to a 4_1^0 transition, which would be FC forbidden in the $\tilde{X}$ state manifold but becomes FC allowed in the $\tilde{B}$ state manifold just like the 4_0^1 transition. It appears that this peak labeled **k** in Fig. 1 was not assigned before because the combination of the hot band and vibronic coupling is necessary to explain this transition. The hot band character is evident now from the cryo-SEVI experiment, while its vibronic coupling origin only becomes clear from the quantum dynamics simulations.

The various contributions from the $\tilde{B}$ state manifold also show intensity above 33 500 cm^{-1} where there is very little intensity seen from the $\tilde{X}$ state manifold. This results in two visible peaks at positions **I** and **J**, which will not disappear at cryogenic temperatures. This is in agreement with experiment as well.

The new cryo-SEVI experiment also offers further data to disentangle the contributions from vibronic coupling between the $\tilde{X}$ and $\tilde{B}$ states by varying the laser frequency near threshold. Thus, Wigner's threshold law[99] can be invoked together with the symmetry rules for allowed detachment channels. It turns out that all FC allowed transitions should result in p-wave electrons having an angular momentum of $l = 1$, while all FC forbidden transitions, which only gain intensity through vibronic coupling to the $\tilde{B}$ state, should produce s-wave electrons with an angular momentum $l = 0$ as was also discussed in Ref. 80. Thus, the energy dependent intensity behavior will scale with $\Delta E^{3/2}$ for $\tilde{X}$ contributions, but with $\Delta E^{1/2}$ for $\tilde{B}$ contributions near threshold. Here, ΔE is the electron kinetic energy depending on the photon energy used. This effect can be taken into account in the present quantum dynamics simulations, and the resulting spectra are presented together with the experimental ones in Fig. 4. In the theoretical simulation, a unique fixed ratio for the contributions of the partial $\tilde{X}$ and $\tilde{B}$ states is used. The variation of the relative peak intensities is only due to the Wigner
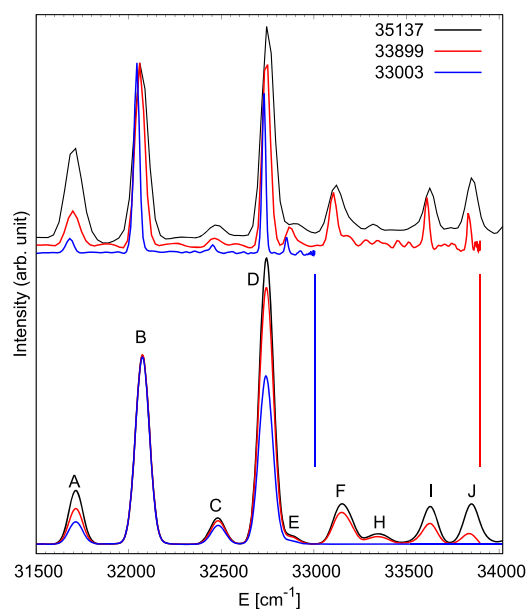

FIG. 4. Experimental (top) and theoretical (bottom) spectra at three photon energies: 35 137 cm^{-1} (black), 33 899 cm^{-1} (red), and 33 003 cm^{-1} (blue). The photon energies are materialized by the vertical red and blue lines. 35 137 cm^{-1} (black) is outside the plotted energy range. The experimental spectra are reproduced from Fig. 3(a) of Ref. 80 with permission from the authors. Both the experimental spectra and the theoretical simulations are scaled such that the maxima of peak **B** are identical for the three photon energies.

energy dependence introduced by the $\Delta E^{3/2}$ and $\Delta E^{1/2}$ additional multiplicative factors.

The first observation seen at first glance is that the intensity pattern is grossly different from the high temperature spectrum. The second very important point is that the theoretical simulation taking the near threshold effects into account are in very good agreement with experiment. To show the agreement more clearly, a direct comparison between experimental spectra and the corresponding simulation is presented for each of the six different photon energies used in the experiment in Fig. 5.

This level of agreement is only possible if the assumptions made for the simulation are reasonable of course, giving evidence for both the assumption of the electron wave character and the vibronic coupling between the $\tilde{X}$ and $\tilde{B}$ states. Surely, this agreement is not and cannot be perfect. One important effect that is not accounted for is the narrowing of the experimental lines when the photon energy is lowered. In the theoretical simulations, the line widths are induced by the damping of the autocorrelation functions before Fourier transformation, while in the experiment, overall rotation and experimental resolution determine the line widths. Only peak intensities are compared in the present context although the Wigner threshold law affects the detachment cross section rather than the intensity. So, in the following discussion, it should be kept in mind that a peak with a smaller half-width will be more intense for the same cross section. The simulation shows the same half-widths regardless of the photon energy contrary to the experimental features.
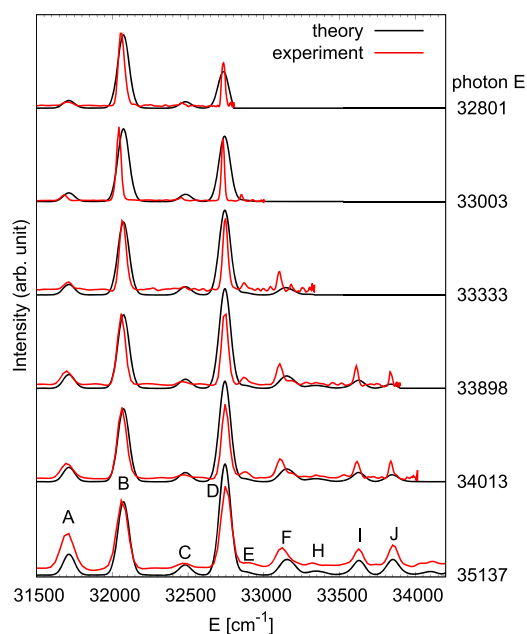
FIG. 5. Experimental (red) and theoretical (black) spectra at various photon energies as given in cm^{-1} along the vertical axis. Experimental[80] and theoretical spectra are scaled such that the maximum of peak **B** is identical. The fixed contribution of the partial $\tilde{X}$ and $\tilde{B}$ states in the theoretical simulation is identical for all six plots. The variation of the relative peak intensities is only due to the Wigner energy dependence.

In the following, the effect of the near threshold detachment is discussed in detail. The most surprising point is that the origin 0_0^0 peak (**A**) by far is not the most intense feature anymore (see Fig. 4). For all but the two lowest photon energies, peak **D** shows the highest intensity. Peak **B** becomes the dominant feature for the two lowest photon energies, followed by **D**. On the contrary, according to a simple standard FC picture, the 0_0^0 transition would be expected as the dominating line of the spectrum because the equilibrium structures of the anion and the radical are very similar. One would also expect this to become even more pronounced when detaching at near threshold, but the contrary is the case. Furthermore, both the **A/B** and **A/D** intensity ratios decrease significantly rather than increasing when the photon energy is reduced. Note that the intensity of all spectra was normalized with respect to peak **B**. The reason for the above observation clearly is the different electron wave character because **B** and **D** are mainly due to the $\tilde{B}$ state and result in s-wave electrons, while **A** is entirely due to the $\tilde{X}$ state corresponding to p-wave electrons. The present detailed quantum dynamics simulations show unequivocally that this effect cannot be reproduced without the vibronic coupling effects between these two electronic states. There would be no contribution from the $\tilde{B}$ state manifold in the energy region of the present study without significant vibronic coupling. This conclusion is the same as in previous theoretical studies[64,80] and is strengthened immensely by the excellent agreement between our detailed simulations of the near threshold effects and the cryo-SEVI experiments.

This agreement is found not only for the **A/B** and **A/D** but also for the **B/D** intensity ratio. In this case, a slight increase is observed when the photon energy is lowered, showing that these two peaks belong to the same electronic state manifold and, thus, l quantum number of the outgoing electrons. It is also clear from the simulations that the corresponding case is $l = 0$ and the intensity of **B** originates dominantly from the $\tilde{B}$ state manifold. This is of particular interest because the assignment of **B** as the FC forbidden 4_0^1 detachment[34,80] has been disputed by Hirota[100] based on the interpretation of Yamada and Ross.[98] However, the present detailed simulation results clearly support the assignment of feature **B** as 4_0^1 detachment. The near threshold results also clearly support another debated assignment, namely, that of peak **D**. It is unequivocal that the main contribution to that feature originates from the $\tilde{B}$ state and corresponds to an FC forbidden 3_0^1 detachment. This was already discussed above when analyzing the partial spectra from the simulations. The FC allowed 1_0^1 detachment predicted close by in energy is suppressed in these near threshold spectra and contributes even less to peak **D** than in the hot spectrum. Even in the 435 K spectrum, 1_0^1 detachment has only a minor effect compared to FC forbidden 3_0^1 detachment, contrary to the initial assignment.

Finally, there is also an interesting observation for peak **C** in both experiment and simulation. The ratio of **A/C** decreases strongly when the photon energy is lowered. This indicates that **A** and **C** correspond to different l quantum numbers for the outgoing electron wave. In fact, the assignment of peak **C** to 4_0^2 detachment turns out to be correct, but the double excitation of a degenerate e' mode leads to a more complex picture for **C** when compared to **A**. The temptation to assume an FC allowed transition corresponding to the $\tilde{X}$ state manifold just like peak **A** does not account for this complexity. Indeed, the present case leads to two different sublevels of a_1' and e' symmetry. These two sublevels are found to be only 20 cm^{-1} apart in energy, and the 4_0^2 (e') sublevel corresponds to an FC forbidden transition allowed by coupling to the $\tilde{B}$ state. The latter sublevel is less affected by the near threshold effect than the FC allowed a_1' sublevel because the corresponding electron wave belongs to $l = 0$ rather than $l = 1$. It appears that in the 435 K spectrum, this peak is dominated by the 4_0^2 (a_1') sublevel, thus having a higher intensity, while in the cryo-SEVI spectrum, this feature is mainly due to the 4_0^2 (e') sublevel resulting in a lower but less photon energy dependent intensity.

V. CONCLUSIONS AND OUTLOOK

A new and highly accurate full-dimensional and fully coupled diabatic potential energy (PES) model is presented for the lowest electronic states of NO$_3$, namely, $\tilde{X}$ ^{2}A$_2'$, $\tilde{A}$ ^{2}E$''$, and $\tilde{B}$ ^{2}E$'$. This model is based on high quality *ab initio* reference data that were diabatized by the recently developed method of complete nuclear permutation inversion invariant artificial neural network (CNPI-ANN) diabatization.[78] A reduced-dimensional model for planar NO$_3$ was extended by adding a second ANN to account for the out-of-plane motion. This model is extremely efficient and reproduces the *ab initio* reference data very accurately. Quantum wavepacket dynamics simulations using this model are performed to study the photodetachment spectroscopy of the NO$_3^-$ anion detaching into the

energetic region of the $\tilde{X}$ state of the radical. These calculations are designed such that the two available experiments, an older recording at elevated temperature[34] and a very recent SEVI spectrum at cryogenic temperature,[80] are reproduced. To this end, the effect of temperature and near threshold effects (Wigner's threshold law) are accounted for. Furthermore, the strong *pseudo*-Jahn–Teller coupling between the $\tilde{X}$ and $\tilde{B}$ states leads to additional contributions in the energetic region of the $\tilde{X}$ state manifold, which contribute considerably to the experimentally observed spectra and are modeled properly in the present simulations. Very good agreement is achieved, giving strong evidence to the interpretation of the detailed theoretical data.

Temperature effects are taken into account in a straightforward way to simulate the contribution of hot bands. To this end, partial spectra are computed for several initial vibrational states of the anion and the total spectrum is obtained as a weighted superposition using the Boltzmann factors for a temperature of 435 K. This does not yield a satisfactory spectrum if only the $\tilde{X}$ state manifold is considered. Therefore, a second set of partial spectra is computed, accounting for the $\tilde{B}$ state manifold and yielding Franck–Condon (FC) forbidden transitions, which become allowed through the strong *pseudo*-Jahn–Teller coupling. Only the weighted superposition of all partial spectra from $\tilde{X}$ state and $\tilde{B}$ state manifold yields a simulated spectrum that agrees with experiment. In fact, the obtained agreement is excellent, giving strong support for the assumptions made in the simulation. The simulations allow us to identify the 0_0^0 transition in agreement with experiment and two hot bands to the red of it, namely, 4_1^1 and 4_1^0. The latter transition is FC forbidden and borrows its intensity from the $\tilde{B}$ state apparently. The first prominent peak to the blue is a superposition of the weak FC allowed 4_1^3 hot band and the much stronger FC forbidden 4_0^1 detachment. The present result hopefully will settle the debate about the corresponding assignments. A further strong experimental feature a bit more than 1000 cm^{-1} above the 0_0^0 line also turns out to be a superposition and a weak FC allowed 1_0^1 detachment and a much stronger FC forbidden 3_0^1 transition that borrows intensity from the $\tilde{B}$ state through vibronic coupling. This yields further support from both experiment and theory that the disputed ν_3 fundamental of neutral NO$_3$ is found around 1040 cm^{-1} rather than at 1492 cm^{-1}.

The evidence for the above assignments is strengthened by the simulation of the new cryo-SEVI spectra in which the near threshold effects (Wigner's threshold law) are taken into account. The two partial spectra for the $\tilde{X}$ and $\tilde{B}$ state correspond to different angular momenta for the detached electrons, $l = 1$ for $\tilde{X}$ and $l = 0$ for $\tilde{B}$. The different threshold behavior allows us to disentangle which peaks are dominated by which electronic state manifold. The cryogenic temperature of 10 K removes all contributions from hot bands. The experimental cryo-SEVI spectra taken at six different photon energies show very different intensity patterns from the 435 K spectrum; yet, they are simulated in very good agreement using the present model. The detailed analysis confirms the above assignments and, furthermore, identifies another peak as a superposition of weak FC allowed 4_0^2 (a_1') and strong FC forbidden 4_0^2 (e') detachment. All these results clearly show the importance of the vibronic coupling between the $\tilde{X}$ and $\tilde{B}$ states without which it would be impossible to simulate the experimental results that well.

Finally, the very good agreement with experiment obtained for all the spectra indicates the accuracy of the underlying diabatic PES model. The model also includes the $\tilde{A}$ state for which at least a photodetachment spectrum at elevated temperature was recorded and published. It can be expected that the present PES model will also yield detailed simulation results for that spectrum and this shall be studied in the near future. Furthermore, the model allows us to investigate the nonadiabatic dynamics after exciting the wavepacket to one of the excited states. This may allow us to disentangle some further experimental observations, like the $\tilde{B}$ state lifetime, which are not well-understood, yet. We hope that the continuous work will lift some more secrets of the enigmatic NO$_3$ radical in the future.

APPENDIX: COORDINATES, INVARIANTS, AND DIAGONAL POTENTIALS OF THE DIABATIC PES MODEL

1. Coordinates Q

The symmetry-adapted coordinates are constructed from a set of primitive valence coordinates as already described in previous works[73,83] and account for the basic asymptotic behavior in the underlying low-order model. The primitive coordinates comprising the three N–O distances r_i and a set of O–N–O angles α_i are first transformed non-linearly as

$$m_i = 1 - \exp(-\gamma(r_i - r_0)), \tag{A1a}$$

$$\alpha_i' = \frac{\alpha_i - \alpha_0}{r_j r_k}, \quad i \ne j \ne k, \tag{A1b}$$

where r_0 and α_0 are the respective distances and angles at the reference point and γ is a chosen Morse parameter. These primitive coordinates are then linearly transformed to yield the symmetry-adapted coordinates a (breathing mode) and the degenerate asymmetric modes x_s, y_s (stretching) and x_b, y_b (bending):

$$a = \sqrt{\frac{1}{3}}(m_1 + m_2 + m_3), \tag{A2a}$$

$$x_s = \sqrt{\frac{1}{6}}(2m_1 - m_2 - m_3), \tag{A2b}$$

$$y_s = \sqrt{\frac{1}{2}}(m_2 - m_3), \tag{A2c}$$

$$x_b = \sqrt{\frac{1}{6}}(2\alpha_1' - \alpha_2' - \alpha_3'), \tag{A2d}$$

$$y_b = \sqrt{\frac{1}{2}}(\alpha_2' - \alpha_3'). \tag{A2e}$$

The symmetry-adapted out-of-plane umbrella coordinate θ is constructed from the trisector angle ϑ as follows:

$$\theta = \frac{\vartheta - \frac{\pi}{2}}{r_1 r_2 r_3}. \tag{A3}$$

2. Invariants $\widetilde{\mathbf{Q}}$

For the sake of simplicity, let $r_{s,b}^2$ be given as

$$r_{s,b}^2 = x_{s,b}^2 + y_{s,b}^2. \tag{A4}$$

Furthermore, let the third order invariant terms τ_{jk} with $j, k \in \{s, b\}$ be defined as

$$\tau_{jk} = x_j^2 x_k - x_k y_j^2 - 2x_j y_k y_j. \tag{A5}$$

$\widetilde{\mathbf{Q}}$ is then composed of the following invariants:

$$\tilde{Q}_1 = a, \tag{A6a}$$

$$\tilde{Q}_2 = r_s^2, \tag{A6b}$$

$$\tilde{Q}_3 = r_b^2, \tag{A6c}$$

$$\tilde{Q}_4 = \theta^2, \tag{A6d}$$

$$\tilde{Q}_5 = x_s x_b + y_s y_b, \tag{A6e}$$

$$\tilde{Q}_6 = 10 \cdot \tanh(0.1 \cdot \tau_{ss}), \tag{A6f}$$

$$\tilde{Q}_7 = 10 \cdot \tanh(0.1 \cdot \tau_{bb}), \tag{A6g}$$

$$\tilde{Q}_8 = 10 \cdot \tanh(0.1 \cdot \tau_{sb}), \tag{A6h}$$

$$\tilde{Q}_9 = 10 \cdot \tanh(0.1 \cdot \tau_{bs}). \tag{A6i}$$

3. Diagonal model terms

The totally symmetric diagonal contributions of the reference model are expressed here in terms of three independent scalar functions $V_i(\mathbf{Q})$,

$$W_{\text{diag}}^d(\mathbf{Q}) = \begin{pmatrix} V_1(\mathbf{Q}) & 0^T & 0^T \\ 0 & V_2(\mathbf{Q})\mathbf{1} & 0 \\ 0 & 0 & V_3(\mathbf{Q})\mathbf{1} \end{pmatrix}. \tag{A7}$$

Apart from the constant terms, referring to the vertical excitation energies at the reference point, an expansion of each $V_i(\mathbf{Q})$, $i = 1$, 2, 3 up to second order yields four (constant) coefficients μ_k^i and corresponding polynomial terms,

$$V_i(\mathbf{Q}) = \mu_1^i \cdot a + \mu_2^i \cdot a^2 + \mu_3^i \cdot r_s^2 + \mu_4^i \cdot r_b^2, \tag{A8}$$

where r_i^2 are defined in Eq. (A4).

DATA AVAILABILITY

The data that support the findings of this study are available from the corresponding author upon reasonable request.

REFERENCES

[1] R. P. Wayne, *Chemistry of Atmospheres*, 3rd ed. (Oxford University Press, Oxford, 2000).

[2] P. Hautefeuille and J. Chappuis, C. R. Acad. Sci. Paris **92**, 80 (1881).

[3] G. Sprenger, Z. Elektrochem. **37**, 674 (1931).

[4] E. J. Jones and O. R. Wulf, J. Chem. Phys. **5**, 873 (1937).

[5] G. Schott and N. Davidson, J. Am. Chem. Soc. **80**, 1841 (1958).

[6] H. S. Johnston and R. Graham, Can. J. Chem. **52**, 1415 (1974).

[7] R. A. Graham and H. S. Johnston, J. Phys. Chem. **82**, 254 (1978).

[8] D. N. Mitchell, R. P. Wayne, P. J. Allen, R. P. Harrison, and R. J. Twin, J. Chem. Soc., Faraday Trans. 2 **76**, 785 (1980).

[9] D. A. Ramsay, Proc. Colloq. Spectrosc. Int. **10**, 583 (1962).

[10] W. J. Marinelli, D. M. Swanson, and H. S. Johnston, J. Chem. Phys. **76**, 2864 (1982).

[11] H. H. Nelson, L. Pasternack, and J. R. McDonald, J. Phys. Chem. **87**, 1286 (1983).

[12] H. H. Nelson, L. Pasternack, and J. R. McDonald, J. Chem. Phys. **79**, 4279 (1983).

[13] T. Ishiwata, I. Fujiwara, Y. Naruge, K. Obi, and I. Tanaka, J. Phys. Chem. **87**, 1349 (1983).

[14] T. Ishiwata, I. Tanaka, K. Kawaguchi, and E. Hirota, J. Chem. Phys. **82**, 2196 (1985).

[15] K. Kawaguchi, E. Hirota, T. Ishiwata, and I. Tanaka, J. Chem. Phys. **93**, 951 (1990).

[16] K. Kawaguchi, T. Ishiwata, I. Tanaka, and E. Hirota, Chem. Phys. Lett. **180**, 436 (1991).

[17] T. Ishiwata, I. Tanaka, K. Kawaguchi, and E. Hirota, J. Mol. Spectrosc. **153**, 167 (1992).

[18] E. Hirota, T. Ishiwata, K. Kawaguchi, M. Fujitake, N. Ohashi, and I. Tanaka, J. Chem. Phys. **107**, 2829 (1997).

[19] K. Kawaguchi, T. Ishiwata, E. Hirota, and I. Tanaka, Chem. Phys. **231**, 193 (1998).

[20] T. Ishiwata, Y. Nakano, K. Kawaguchi, E. Hirota, and I. Tanaka, J. Phys. Chem. A **114**, 980 (2010).

[21] K. Kawaguchi, N. Shimizu, R. Fujimori, J. Tang, T. Ishiwata, and I. Tanaka, J. Mol. Spectrosc. **268**, 85 (2011).

[22] R. Fujimori, N. Shimizu, J. Tang, T. Ishiwata, and K. Kawaguchi, J. Mol. Spectrosc. **283**, 10 (2013).

[23] K. Kawaguchi, R. Fujimori, J. Tang, and T. Ishiwata, J. Phys. Chem. A **117**, 13732 (2013).

[24] K. Tada, W. Kashihara, M. Baba, T. Ishiwata, E. Hirota, and S. Kasahara, J. Chem. Phys. **141**, 184307 (2014).

[25] K. Tada, K. Teramoto, T. Ishiwata, E. Hirota, and S. Kasahara, J. Chem. Phys. **142**, 114302 (2015).

[26] E. Hirota, J. Mol. Spectrosc. **310**, 99 (2015).

[27] K. Kawaguchi, R. Fujimori, J. Tang, and T. Ishiwata, J. Mol. Spectrosc. **314**, 73 (2015).

[28] K. Tada, T. Ishiwata, E. Hirota, and S. Kasahara, J. Mol. Spectrosc. **321**, 23 (2016).

[29] K. Kawaguchi, T. Narahara, R. Fujimori, J. Tang, and T. Ishiwata, J. Mol. Spectrosc. **334**, 10 (2017).

[30] M. E. Jacox and W. E. Thompson, J. Chem. Phys. **129**, 204306 (2008).

[31] H. Beckers, H. Willner, and M. E. Jacox, Chem. Phys. Chem. **10**, 706 (2009).

[32] M. E. Jacox and W. E. Thompson, J. Phys. Chem. A **114**, 4712 (2010).

[33] R. R. Friedl and S. P. Sander, J. Phys. Chem. **91**, 2721 (1987).

[34] A. Weaver, D. W. Arnold, S. E. Bradforth, and D. M. Neumark, J. Chem. Phys. **94**, 1740 (1991).

[35] B. Kim, P. L. Hunter, and H. S. Johnston, J. Chem. Phys. **96**, 4057 (1992).

[36] R. T. Carter, K. F. Schmidt, H. Bitto, and J. R. Huber, Chem. Phys. Lett. **257**, 297 (1996).

[37] J. Orphal, C. E. Fellows, and P.-M. Flaud, J. Geophys. Res.: Atmos. **108**, 4077, https://doi.org/10.1029/2002jd002489 (2003).

[38] A. Deev, J. Sommar, and M. Okumura, J. Chem. Phys. **122**, 224305 (2005).

[39] K. Takematsu, N. C. Eddingsaas, D. J. Robichaud, and M. Okumura, Chem. Phys. Lett. **555**, 57 (2013).

[40] T. Codd, M.-W. Chen, M. Roudjane, J. F. Stanton, and T. A. Miller, J. Chem. Phys. **142**, 184305 (2015).

[41] T. E. H. Walker and J. A. Horsley, Mol. Phys. **21**, 939 (1971).

[42] A. Lund and K.-Å. Thuomas, Chem. Phys. Lett. **44**, 569 (1976).

[43] J. F. Olsen and L. Burnelle, J. Am. Chem. Soc. **92**, 3659 (1970).

[44] N. C. Baird and K. F. Taylor, Chem. Phys. Lett. **80**, 83 (1981).

[45] P. E. M. Siegbahn, J. Comput. Chem. **6**, 182 (1985).

[46] B. Kim, H. S. Johnston, D. A. Clabo, Jr., and H. F. Schaefer III, J. Chem. Phys. **88**, 3204 (1988).

[47] R. C. Boehm and L. L. Lohr, J. Phys. Chem. **93**, 3430 (1989).

[48] R. C. Boehm and L. L. Lohr, J. Comput. Chem. **12**, 119 (1991).

[49] R. D. Davy and H. F. Schaefer III, J. Chem. Phys. **91**, 4410 (1989).

[50] B. Kim, B. L. Hammond, W. A. Lester, Jr., and H. S. Johnston, Chem. Phys. Lett. **168**, 131 (1990).

[51] V. R. Morris, S. C. Bhatia, and J. H. Hall, Jr., J. Phys. Chem. **94**, 7414 (1990).

[52] V. R. Morris, S. C. Bhatia, and J. H. Hall, Jr., J. Phys. Chem. **95**, 9203 (1991).

[53] J. F. Stanton, J. Gauss, and R. J. Bartlett, J. Chem. Phys. **94**, 4084 (1991).

[54] J. F. Stanton, J. Gauss, and R. J. Bartlett, J. Chem. Phys. **97**, 5554 (1992).

[55] U. Kaldor, Chem. Phys. Lett. **166**, 599 (1990).

[56] U. Kaldor, Chem. Phys. Lett. **185**, 131 (1991).

[57] A. Stirling, I. Pápai, J. Mink, and D. R. Salahub, J. Chem. Phys. **100**, 2910 (1994).

[58] L. A. Eriksson, J. Wang, R. J. Boyd, and S. Lunell, J. Phys. Chem. **98**, 792 (1994).

[59] T. D. Crawford, T. J. Lee, N. C. Handy, and H. F. Schaefer III, J. Chem. Phys. **107**, 9980 (1997).

[60] C. D. Sherrill, M. S. Lee, and M. Head-Gordon, Chem. Phys. Lett. **302**, 425 (1999).

[61] W. Eisfeld and K. Morokuma, J. Chem. Phys. **113**, 5587 (2000).

[62] W. Eisfeld and K. Morokuma, J. Chem. Phys. **114**, 9430 (2001).

[63] W. Eisfeld and K. Morokuma, J. Chem. Phys. **117**, 4361 (2002).

[64] M. Mayer, L. S. Cederbaum, and H. Köppel, J. Chem. Phys. **100**, 899 (1994).

[65] J. F. Stanton, J. Chem. Phys. **126**, 134309 (2007).

[66] M. Okumura, J. F. Stanton, A. Deev, and J. Sommar, Phys. Scr. **73**, C64 (2006).

[67] J. F. Stanton, Mol. Phys. **107**, 1059 (2009).

[68] J. F. Stanton and M. Okumura, Phys. Chem. Chem. Phys. **11**, 4742 (2009).

[69] C. S. Simmons, T. Ichino, and J. F. Stanton, J. Phys. Chem. Lett. **3**, 1946 (2012).

[70] Z. Homayoon and J. M. Bowman, J. Chem. Phys. **141**, 161104 (2014).

[71] S. Mahapatra, W. Eisfeld, and H. Köppel, Chem. Phys. Lett. **441**, 7 (2007).

[72] S. Faraji, H. Köppel, W. Eisfeld, and S. Mahapatra, Chem. Phys. **347**, 110 (2008).

[73] W. Eisfeld, O. Vieuxmaire, and A. Viel, J. Chem. Phys. **140**, 224109 (2014).

[74] W. Eisfeld and A. Viel, J. Chem. Phys. **146**, 034303 (2017).

[75] A. Viel and W. Eisfeld, Chem. Phys. **509**, 81 (2018).

[76] D. M. G. Williams and W. Eisfeld, J. Chem. Phys. **149**, 204106 (2018).

[77] D. M. G. Williams, A. Viel, and W. Eisfeld, J. Chem. Phys. **151**, 164118 (2019).

[78] D. M. G. Williams and W. Eisfeld, J. Phys. Chem. A **124**, 7608 (2020).

[79] A. D. Walsh, J. Chem. Soc. **1953**, 2301–2306.

[80] M. C. Babin, J. A. DeVine, J. DeWitt, J. F. Stanton, and D. M. Neumark, J. Phys. Chem. Lett. **11**, 395 (2020).

[81] A. Viel and W. Eisfeld, J. Chem. Phys. **120**, 4603 (2004).

[82] W. Eisfeld and A. Viel, J. Chem. Phys. **122**, 204317 (2005).

[83] A. Viel, W. Eisfeld, S. Neumann, W. Domcke, and U. Manthe, J. Chem. Phys. **124**, 214306 (2006).

[84] W. Eisfeld, J. Chem. Phys. **134**, 054303 (2011).

[85] F. Venghaus and W. Eisfeld, J. Chem. Phys. **144**, 114110 (2016).

[86] N. Wittenbrink, F. Venghaus, D. Williams, and W. Eisfeld, J. Chem. Phys. **145**, 184108 (2016).

[87] T. Weike, D. M. G. Williams, A. Viel, and W. Eisfeld, J. Chem. Phys. **151**, 074302 (2019).

[88] H. Köppel, W. Domcke, and L. S. Cederbaum, Adv. Chem. Phys. **57**, 59 (1984).

[89] *Conical Intersections: Electronic Structure, Dynamics and Spectroscopy* edited by W. Domcke, D. R. Yarkony, and H. Köppel, (World Scientific, Singapore, 2004).

[90] H. J. Werner and P. J. Knowles, J. Chem. Phys. **89**, 5803 (1988).

[91] P. J. Knowles and H.-J. Werner, Chem. Phys. Lett. **145**, 514 (1988).

[92] MOLPRO 2009.1 Is a Package of ab Initio Programs Written by H.-J. Werner, P. J. Knowles, R. Lindh, F. R. Manby, M. Schütz *et al.*, see http://www.molpro.net.

[93] H.-D. Meyer, U. Manthe, and L. S. Cederbaum, Chem. Phys. Lett. **165**, 73 (1990).

[94] U. Manthe, H. D. Meyer, and L. S. Cederbaum, J. Chem. Phys. **97**, 3199 (1992).

[95] U. Manthe, J. Chem. Phys. **128**, 064108 (2008).

[96] C. Evenhuis, G. Nyman, and U. Manthe, J. Chem. Phys. **127**, 144302 (2007).

[97] U. Manthe, J. Chem. Phys. **105**, 6989 (1996).

[98] K. Yamada and S. Ross, in *96th Annual Meeting of the Chemical Society of Japan*, edited by K. Kyotanabe (The Chemical Society of Japan, 2016) Japan pp. Paper 2E6–28.

[99] E. P. Wigner, Phys. Rev. **73**, 1002 (1948).

[100] E. Hirota, J. Mol. Spectrosc. **343**, 81 (2018).